4-28-1994

Quantitative Dark-Field Mass Analysis of Ultrathin Cryosections in the Field-Emission Scanning Transmission Electron Microscope

S. Brian Andrews
National Institute of Neurological Disorders and Stroke

Roger A. Buchanan
National Institute of Neurological Disorders and Stroke

Richard D. Leapman
National Institutes of Health, Bethesda

Follow this and additional works at: https://digitalcommons.usu.edu/microscopy

Part of the Biology Commons

Recommended Citation

Utah State University
MERRILL-CAZIER LIBRARY

QUANTITATIVE DARK-FIELD MASS ANALYSIS OF ULTRATHIN CRYOSECTIONS IN THE FIELD-EMISSION SCANNING TRANSMISSION ELECTRON MICROSCOPE

S. Brian Andrews[1][*], Roger A. Buchanan[1] and Richard D. Leapman[2]

[1]Laboratory of Neurobiology, National Institute of Neurological Disorders and Stroke, and
[2]Biomedical Engineering & Instrumentation Program, National Center for Research Resources, National Institutes of Health, Bethesda, MD 20892-4062.

Abstract

The availability of a cryotransfer stage, highly efficient electron energy loss spectrometers, and ultrathin-window energy-dispersive x-ray spectrometers for the VG Microscopes HB501 field-emission scanning transmission electron microscope (STEM) provides this instrument with the potential for high resolution biological microanalysis. Recent technical advances offer cryosections that are thin enough to take advantage of the analytical capabilities of this microscope. This paper first discusses the quantitative characterization of freeze-dried, ultrathin cryosections of directly frozen liver and brain by low-dose dark-field STEM imaging. Such images reveal high-quality sections with good structural detail, mainly due to reduced preparation artifacts and electron beam damage. These sections are thin enough for dark-field mass analysis, so that the mass of individual organelles can be measured *in situ*, and their water content deduced. This permits the measurement of mass loss-corrected subcellular elemental concentrations. The results suggest several new applications for cryosections as illustrated by data on synaptic activity-dependent calcium regulation in Purkinje cells of mouse cerebellum. Low-dose mass analysis of cryosections in combination with x-ray and electron spectroscopy is a promising approach to quantitating physiological changes in mass distribution and elemental composition.

Key Words: cryosections, scanning transmission electron microscopy, electron beam damage, cerebellum, dendritic spines, endoplasmic reticulum, electron probe microanalysis

*Address for correspondence:
S.B. Andrews
Bldg. 36, Rm 2A-21, National Institutes of Health,
Bethesda, MD 20892-4062 USA
Phone Number: (301) 496-1296
Fax Number: (301) 480-1485

Introduction

The first scanning transmission electron microscope (STEM) was described over twenty years ago by Crewe and his colleagues (Crewe and Wall, 1970). During the intervening two decades, this microscope has developed into an important tool for characterizing biological structures, so that the STEM equipped with a field-emission gun is now a well established instrument for accurate determination of molecular mass ("mass mapping") (Engel, 1978; Wall, 1979; Wall and Hainfeld, 1986), as well as for high-resolution microanalysis (Isaacson and Johnson, 1975; Colliex, 1985). Recently, the utility of the STEM for biological studies has been enhanced by the development of low-temperature devices to optimize sample stability, and of highly efficient detectors to optimize the weak signals that originate from small biological structures. Thus, a cryotransfer/cold stage (Nicholls and Bovey, 1989), dark-field detector system (Hunt, 1989), parallel-detection electron energy loss spectrometer (EELS) (Krivanek *et al.*, 1989), and high-efficiency energy-dispersive x-ray spectrometer (EDXS) can now be fitted to an instrument like the VG Microscopes HB501 field-emission STEM in our laboratory. We have recently described the improved performance attainable in such a STEM (Leapman and Andrews, 1991, 1992), particularly with regard to recording low-dose dark-field images of freeze-dried biological specimens with little or no electron beam damage, and to analyzing the elemental content of such specimens at near-single-atom sensitivity. Now, technical advances reported recently (Michel *et al.*, 1992; Buchanan *et al.*, 1993) can provide cryosections of directly frozen tissues that are thin enough and have enough structural detail to take advantage of the imaging and analytical capabilities of the modern STEM. In essence, this means that many of the approaches previously considered as limited to isolated molecules or small assemblies, e.g., the mapping of molecular weight distributions or the analysis of a small

number of atoms, can now be applied to subcellular structures *in situ*.

In the present paper we review how improved ultrathin cryosections, in combination with the dark-field imaging capability of a field-emission STEM, can provide new types of information about the composition of biological specimens. We also discuss in detail several important subtleties pertaining to the application of dark-field STEM to cryosections. Lastly, new data on the water and element content of subcellular organelles in liver and brain are presented, with an eye toward understanding calcium regulation by the endoplasmic reticulum. For a detailed discussion of the parallel EELS component of this STEM, the reader is referred to the companion paper by Leapman *et al.* (1994).

Instrumentation

Electron microscope

The instrument used for this study was a VG Microscopes HB501 STEM equipped with a cold field-emission source and a gun lens in addition to a high-excitation objective and two condenser lenses (Leapman and Andrews, 1991). The microscope was operated at 100 keV. The gun vacuum was maintained at about 3×10^{-9} Pa and the specimen chamber vacuum at about 3×10^{-7} Pa. For dark-field imaging the probe current could be reduced to the picoampere range by increasing the second condenser lens excitation and thereby reducing the effective source demagnification. For analytical work at very high dose the probe current was increased to >5nA by exciting both the first and second condenser lenses. Cryotransfer of the frozen hydrated samples at about -175°C into the specimen chamber of the HB501 STEM has been described previously (Andrews and Leapman, 1989). The temperature of the stage could be accurately controlled so that specimens could be slowly freeze-dried; after re-cooling the sample and allowing for thermal equilibrium to be reached, the mechanical drift was less than 0.04 nm/s. STEM micrographs were recorded with an annular dark-field detector, as described below. A detailed discussion and block diagram of this STEM are provided elsewhere. (Leapman and Andrews, 1991; Leapman *et al.*, 1994).

Dark-field detector system

Weights of macromolecules were determined from scattering intensities in low-dose, dark-field STEM images (Wall and Hainfeld, 1986). The annular dark-field detector was a single-crystal YAG scintillator with a 4 mm inner diameter and a 12 mm outer diameter. The effective collection angle for elastic scattering was

Fig. 1. Low-dose, low-temperature dark-field STEM image of microtubule (right), tobacco mosaic virus particle (left, for mass calibration), and single squid brain kinesin molecule (arrows) attached to approximately 3 nm-thick carbon substrate. This contrast-enhanced image reveals kinesin as a bilobed structure (arrows) with thin connecting stalk (between arrows); boundaries of three structural domains can readily be approximated. Analysis of molecular masses of domains was based on the average of numerous correlated images. Conditions for dark-field mass analysis: probe size < 1 nm; dose < 1000 e/nm² at 100 kV; resolution = 1.9 nm/pixel. Bar = 25 nm.

Fig. 2. Low magnification dark-field STEM image of freeze-dried cryosection of directly frozen mouse cerebellum. This field illustrates the limited extent of compression and freeze-drying in good preparations. Organization of the neuropil is not evident at this magnification; except for nucleus at upper-left, mitochondria-rich cross-sections of dendrites (arrows) are the only obvious structural feature. Pixel size = 40 nm. Bar = 5 μm.

Fig. 3. Contrast-reversed dark-field STEM image of freeze-dried cryosection of directly frozen mouse cerebellum. Cross-section of dendrite contains both longitudinal and cross-sectional profiles of endoplasmic reticulum (arrowheads), some of which are wrapped around mitochondria. This micrograph well illustrates structures—mitochondria, endoplasmic reticulum, and cytoplasm—which were analyzed by EDXS. Pixel size = 10 nm. Bar = 250 nm.

Fig. 4. Low-dose dark-field STEM images of freeze-dried cryosection of unfixed, directly frozen mouse liver at high magnification. Image has been contrast-reversed and enhanced. Several mitochondria and stacks of endoplasmic reticulum are seen in the perinuclear region of this hepatocyte. Membrane and lumen of endoplasmic reticulum are clearly differentiated; dense cytoplasmic matrix is rich in filamentous and globular components, as well as in other membrane profiles. Pixel size = 10 nm. Bar = 250 nm.

typically 20–60 mrad. Single-electron pulses generated by the scintillator and photomultiplier were amplified, discriminated and fed into a fast counter in the computer (Hunt, 1989). Pulses could be counted at rates ≥ 2 MHz and pixel dwell times of 100 μs were possible. Thus, images containing 512x512 pixels could be recorded in 25 s. Images were transferred to an Apple Macintosh II computer for analysis by means of the
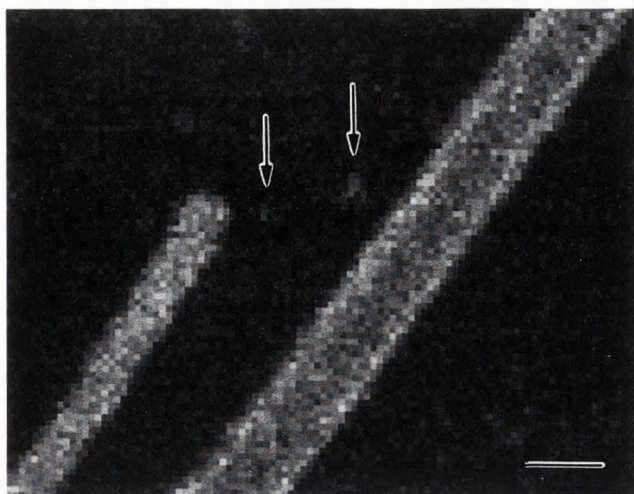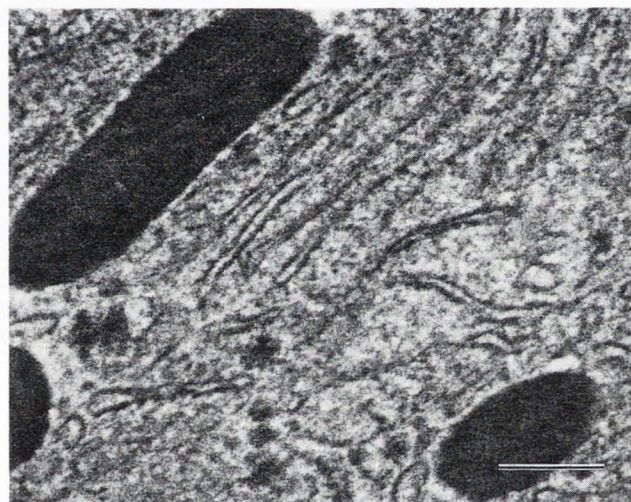
1
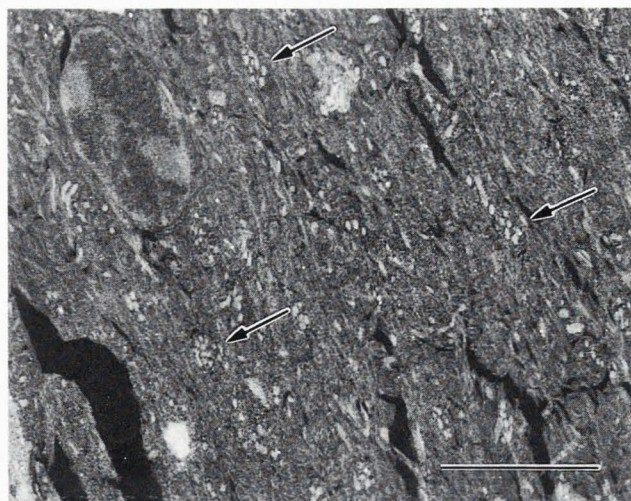
2

3

4

image processing program, *IMAGE*, written at the National Institutes of Health by W.S. Rasband and available from the author.

Spectrometers

Energy-dispersive x-ray spectroscopy (EDXS) was performed by means of a Tracor Northern Micro-ZHV ultrathin-window detector (solid angle approximately 0.18 sterad) and a Tracor Northern TN5500 multichannel analyzer and microanalysis system (Leapman and Andrews, 1991). The thin-window design permits detection of the light elements carbon, nitrogen and oxygen. For x-ray analysis it was necessary to remove the objective aperture and insert the virtual objective aperture in order to avoid spurious x-ray generation. X-ray spectra were transferred to an Apple Macintosh II

computer and processed using the program *DeskTop Spectrum Analyzer* (*DTSA*) (Fiori and Swyt, 1992). The quantification procedure is based on multiple least-squares fitting and the Hall peak/continuum method (Hall and Gupta, 1983; Kitazawa *et al.*, 1983).

Electron energy loss spectroscopy (EELS) measurements were carried out using a Gatan Model 666 parallel-detection spectrometer specially modified for ultrahigh-vacuum compatibility (Krivanek *et al.*, 1989). This spectrometer is fully described elsewhere (Leapman and Andrews, 1992; Leapman *et al.*, 1993).

Advances in Dark-Field Imaging and Analysis

The main applications of STEM over the past decade have involved molecular weight measurement,

a technique established by Wall (1979), Engel (1978), Wall and Hainfeld (1986) and others. This so-called mass mapping technique is based on the fact that the elastic scattering intensity at any pixel is directly proportional to the projected molecular mass. The constant of proportionality is the same for all proteins and nucleotides. Mass mapping in the STEM can be performed at low electron doses (about 10^3 e/nm^2) because the elastic signal is collected very efficiently with the annular dark-field detector at almost single-electron sensitivity. A unique feature of this technique is that it not only provides the total molecular weight of a structure but also reveals how its mass is distributed within specific domains. The best resolution currently attainable is effectively limited by the specimen preparation and radiation damage to about 2 nm.

To optimize the information retained in the specimen, mass analysis is preferably carried out on rapidly frozen, freeze-dried preparations of purified macromolecules or molecular assemblies. Therefore, improvements in low-temperature sample preparation techniques (Wall and Hainfeld, 1986; Dubochet *et al.*, 1988; Glaeser *et al.*, 1991) have significantly increased the scope of dark-field STEM analysis. The recent availability of cryo-devices to preserve the molecules during transfer and irradiation (Nicholls and Bovey, 1989), as well as the development of optimized annular dark-field detection systems (Hunt, 1989) have also been major technical improvements.

The sensitivity now achievable with current instrumentation is illustrated by our recent study on the conformation of the cytoplasmic motor protein kinesin (Andrews *et al.*, 1993). Squid brain kinesin is the original member of a family of cytoplasmic ATPases which play essential roles in intracellular transport [for a review, see (Goldstein, 1991)]. Dark-field STEM imaging of squid kinesin—a tetrameric, rod-shaped protein with lobed ends and an expected molecular weight of about 370 kD—was used to reveal directly the anticipated three-domain structure of kinesin. Single tetramers of kinesin were found to have a molecular weight of 379 ± 15 kD, consistent with the known amino acid sequence. STEM images (Fig. 1) clearly revealed the distribution of mass among the head, stalk and tail regions of the molecules. Quantitative mass analysis of these domains, averaged over many images, specified the motor and organelle-binding ends of the molecule, and indicates that the visually evident stalk region (Fig. 1) represents 52 kD of a single coiled-coil α-helix. Thus, the sensitivity of mass mapping, which can be as good as 0.5 kD/count at a resolution of 2 nm, is sufficient to provide quantitative conformational information about the tertiary and quaternary structures of even single, moderately-sized molecules. This level of resolution makes STEM a useful counterpart to atomic-resolution structural methods such as NMR and x-ray crystallography.

Application of Dark-Field STEM to Cryosections

Characterization and structural analysis

It is now possible to routinely prepare thin, minimally compressed cryosections of unfixed, directly frozen tissues which retain structural detail comparable to conventional preparations, even at the level of single organelles (Michel *et al.*, 1992). We have recently reported that low-dose, dark-field imaging in the field-emission STEM—essentially as developed for protein molecules (Wall, 1979) and discussed in the previous section—is also a useful technique for mass mapping cryosections (Buchanan *et al.*, 1993). This section discusses some important and occasionally subtle details concerning the application of mass mapping techniques to freeze-dried cryosections.

The best cryosections are cut at microtome settings of < 100 nm, empirically choosing the lowest setting that is compatible with achieving consistent section thickness, i.e., cutting a ribbon of sections. Some of the major advantages and disadvantages of such cryosections can be seen in low-power digital micrographs such as the field of cerebellar cortex shown in Fig. 2. (The organization of the molecular layer and the physiology of this tissue are discussed in the following section.) Only contrast enhancement in the computer was required to extract this image from the raw dark-field data; the latter was acquired precisely like images of molecules (except for the lower resolution). Some characteristic artifacts of these sections are evident—they are clearly compressed (cutting direction left-to-right in Fig. 2), but not intolerably so, and additional shrinking has occurred during drying of the adhered section, as indicated by the numerous and large cracks in the section. Our freeze-drying protocol, previously described (Leapman and Andrews, 1991) involves slowly warming the cryotransferred sections to about -90°C over 4-6h and maintaining them at this temperature for several hours (3h to overnight) before recooling for imaging and analysis. The effects of various freeze-drying protocols have not been investigated.

We and others have recently reported rough but quantitative estimates of the extent of distortion during sectioning (Michel *et al.*, 1992; Buchanan *et al.*, 1993) and drying (Buchanan *et al.*, 1993). These studies indicate that it is not unusual to compress the sections by 50% in the direction of cutting, so that if the compression is compensated by increasing the section thickness,
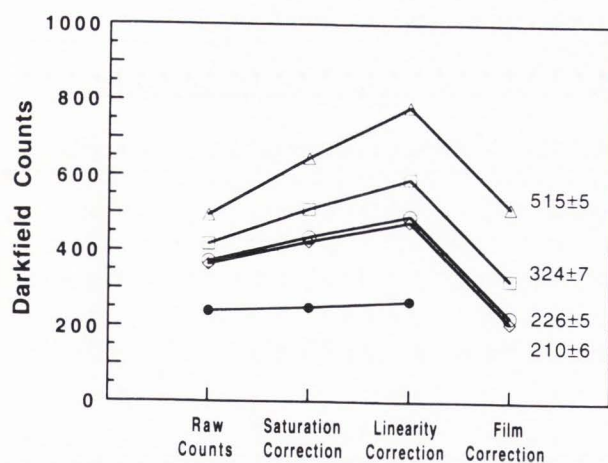
Fig. 5. Sequential correction of raw dark-field counts to account for detector response function, thickness-dependent non-linearity, and support film contribution. Compartments of Purkinje cell dendrites analyzed were mitochondria ($\triangle$), endoplasmic reticulum ($\square$), large fields of neuropil ($\bigcirc$), cytoplasm ($\diamond$), and support film ($\bullet$). Values on plot indicate absolute counts $\pm$ SEM after final correction.
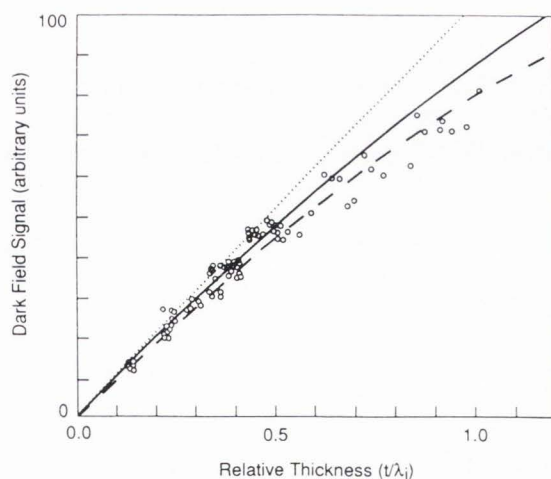

Fig. 6. Dark-field counts versus relative specimen thickness in terms of inelastic mean free path, t/λ_i. (Dashed line) – Theoretical curve with $\lambda_i/\lambda_e = 0.74$ fits experimental measurements (o) from multiply-folded carbon film. (Solid line) – Predicted curve for carbon, scaled to fit experimental data assuming that $\lambda_i/\lambda_e = 0.56$. (Dotted line) – Linear approximation. From Buchanan et al., (1993).

actual section thickness will approach 200 nm (see below). Despite these problems, the section presents large, flat, well-attached fields of tissue in which cellular structures are evident. At higher resolution, structures are easy to identify, especially if the contrast is reversed

so that images appear like conventionally stained electron micrographs (Figs. 3 and 4). Thus, processed low-dose dark-field micrographs of the cerebellar neuropil reveal all of the essential organelles of Purkinje cell dendritic processes (Fig. 3), and similar, higher-magnification micrographs of the perinuclear region of a liver cell (Fig. 4) display subcellular structure at a level comparable to conventional plastic sections.

The quality of these dark-field images depends heavily on the thickness of the cryosection, as is evidenced by the better detail in the thinner liver section (Fig. 4) than in the somewhat thicker brain section (Fig. 3). A recent paper from our laboratories (Buchanan et al., 1993) addressed the issue of section thickness by means of three independent approaches: t/λ_i (thickness/inelastic mean free path) measurements by EELS, dark-field mass measurements in comparison to a thickness standard, and stereoscopic measurements on platinum replicas. Although the results varied from section-to-section, good sections are < 200 nm thick when frozen-hydrated and ≤ 100 nm after drying. Since this corresponds to a thickness of approx. $0.5 \, t/l_i$ (at 100 kV) (Sun et al., 1993), the specimens are well within the single scattering regime, as is necessary for obtaining crisp images.

The thickness of the specimen is even more critical for quantitative analysis of dark-field images, because the direct proportionality between the number of dark-field counts and specimen mass breaks down when plural scattering becomes significant (Colliex et al., 1984; Engel and Reichelt, 1984; Reichelt and Engel, 1986). Given the fact that the dry mass content of tissue structures covers a wide range (about 5 to 50 g/100 g), even the thinnest available cryosections will have dense regions that diverge somewhat from a simple linear relationship. Moreover, other factors need to be considered in order to extract accurate, tissue-specific dark-field counts from the raw image data; these include an instrumental correction for the response of the detection system and a correction for the specimen support. Fig. 5 illustrates the sequential effect of such corrections on a data set from a Purkinje cell dendrite (e.g., Fig. 3) which is on the thicker side of the acceptable range.

Although our annular dark-field detection system will count at rates in excess of 2 MHz, the output begins to show non-linearity at about 0.5 MHz. The response function is empirically well modeled by a quadratic equation; to obtain corrected images, this function is automatically applied on a pixel-by-pixel basis to the raw count data. A second correction is required on account of the thickness effects discussed above. The onset of non-linearity is evident in a plot of the dark-field signal as a function of t/λ_i, the thickness expressed in units of

the inelastic mean free path (Fig. 6). Experimental measurements were obtained from a folded carbon film (Fig. 6, open circles). The dashed line is the predicted behavior based on the fundamental equation for the intensity of scattered electrons, *I*:

$$I = a[1\text{-}\exp(-kz)] \qquad (1)$$

where *k* is the ratio of inelastic to elastic mean free paths

$$k = \lambda_i / \lambda_e \qquad (2)$$

and

$$z = t/\lambda_i \qquad (3)$$

For an appropriate choice of the constant, *a*, the agreement with experimental data is quite good assuming that $k = 0.74$ (Colliex *et al.*, 1984). Using a value of $k = 0.56$ for a dried cryosection (Colliex *et al.*, 1984), one obtains the solid curve in Fig. 6. These results show that for very thin specimens the dark-field signal varies linearly with specimen thickness but as t/λ_i increases to 0.8, departures from linearity approach 20% (e.g., mitochondria in Fig. 5). A procedure for converting the raw intensity, *I*, for this effect has previously been described (Buchanan *et al.*, 1993), as follows:

$$I' = (I_{cal}/a) \ln [1 - a(I/I_{cal})]^{-1} \qquad (4)$$

where

$$a = 1 - \exp [-z_{cal} k] \qquad (5)$$

In these expressions *I'* is the corrected intensity, and the subscript *cal* indicates values from a standard of known relative thickness, in this case the carbon/formvar support at low dose. It can be seen that the factor *a* is a constant depending only on the standard; thus, this procedure can be viewed as calibrating the counts from the tissue according to the relative thickness of a standard, z_{cal}, as measured by EELS. z_{cal} is typically ≈ 0.25 or less, so *a* is on the order of 0.15. Thus, this correction could reasonably be ignored up to $z = 0.5$, at which point the error exceeds 15% (Fig. 6). In practice, the correction is transparently calculated for all values within the data processing spreadsheet. Lastly, the contribution of the support film must be subtracted. In addition to the usual disadvantages of thicker support films, it can be seen that significant counts from the support will increase the size of corrections made in the previous two steps. Thus, quantitative dark-field STEM especially benefits from thin supports.

Table 1. Dry mass of organelles in cryosections as determined by low-dose dark-field STEM[*]

Dry mass content (g/100g wet tissue)[†]		
	Purkinje cell dendrite	Liver cells
Whole tissue	20.0	22.0
Mitochondria	45.6±0.4	35.2±0.5
Endoplasmic reticulum	28.6±0.6	24.0±0.6
Cytoplasm	18.6±0.5	20.6±0.5

[*] Data from single representative images. Errors reported as ±SEM. Data recorded at -160° C with dose of <1000 e/nm².
[†] Values derived from dark-field count data by using the whole image, i.e., cerebellar neuropil and liver parenchyma (literature dry mass contents 20 and 22 g/100 g, respectively) as internal standards. Details discussed in the text.

Mass analysis

The ability to obtain accurate dark-field counts on individual structures in rapidly frozen cryosections raises the possibility of directly measuring, without specimen damage, the masses of cell constituents *in situ*. If an internal standard analogous to tobacco mosaic virus were available, absolute mass values could be calculated exactly as for isolated molecules. In the absence of such a standard, the *relative* masses are still accurately known, and an estimate of *absolute* mass is possible if one invokes alternative calibration procedures. We have evaluated an approach which calibrates organelle-level dark-field counts to averaged counts taken over large, low-magnification image fields, under the assumption that the averaged data should correlate with the dry mass content available from chemical or gravimetric measurements. As shown in Table 1, this method gives plausible values with good precision, implying that this is a reasonable approach.

The ready determination of the absolute mass of organelles and other subcellular structures points to several new, potentially important, applications in cell physiology. Among the more useful is the indirect calculation of water content, on the assumption that the sum of the mass fraction plus the water fraction is equal to one. Changes in water and mass fractions are of immediate interest in several areas of biology, e.g., for tissues whose activity or pathology necessarily involves
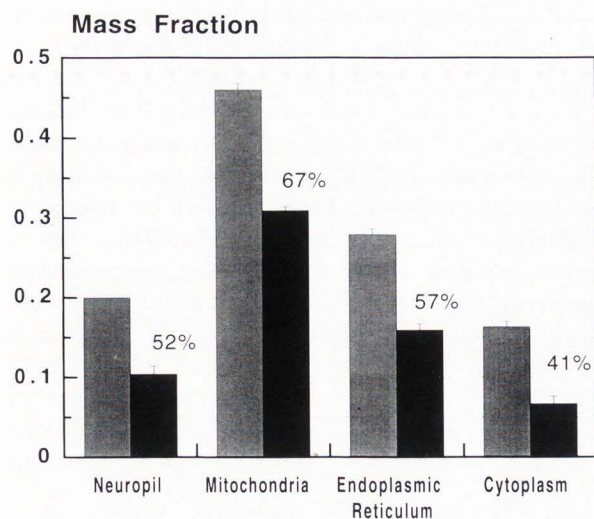
Mass Fraction

Fig. 7. Histogram showing dry mass fractions of various regions and organelles of Purkinje cell dendrites at low dose (<1000 e/nm^2, gray bars) and after high-dose microanalysis (about 10^8 e/nm^2, black bars). Percentages indicate fraction of mass retained after analysis.
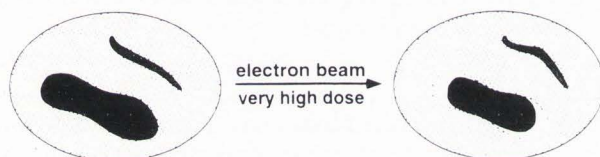

Fig. 8. Schematic illustration of changes in shape and location of organelles that can accompany high-dose exposure of unfixed and unstabilized freeze-dried cryosections. Two common occurrences—mitochondrial shrinkage and membrane movement—are indicated. Consequences of these artifacts are discussed in text.

water movement or for comparing isolated organelles with organelles *in situ*. Although the dark-field method for determining water content is useful, it is indirect, as are most other approaches (von Zglinicki, 1991; Gupta and Hall, 1981; Zierold, 1988). Thus, the recently described method for direct measurement of organelle water on frozen hydrated sections by analyzing the valence band region of the EELS spectrum (Sun *et al.*, 1993) is very promising.

Another interesting application for mass measurements of biological specimens concerns electron beam damage. Low-dose dark-field images are typically obtained at doses <100 electrons/nm^2. Doses of approximately 1000 electrons/nm^2 would appear to be near the threshold for electron beam-induced damage (Isaacson, 1977) to the structure of unfixed and unstabilized cells. In fact, a further increase above approxi-

mately 1000 electrons/nm^2 is sufficient to induce visible damage to the cytoplasm, which appears to begin by collapse of the cytoskeleton. At the much higher doses required for EDXS or EELS analysis, *viz.*, >10^8 electrons/nm^2, beam-induced damage is severe. Dark-field mass mapping can be used to quantify mass loss by comparing the masses of specific organelles before and after beam damage (Fig. 7). However, such comparisons must be carried out with care, since very high dose beam exposure can occasionally induce gross structural changes in addition to terminal mass loss. Two common types of changes—organelle collapse and organelle displacement—are schematically illustrated in Fig. 8. Even in cases where severe shrinkage or movement occurs, however, good results can still be obtained by redrawing the organelle outline in the post-damage image to conform to its new dimensions. Comparison of low-dose and high-dose images revealed differential mass loss between compartments of a Purkinje cell dendrite; for example, the fraction of mass lost from a region of cytoplasm was on average much greater than loss from a typical mitochondrion. How these differences effect the results of elemental analyses is discussed in the next section.

Dark-Field Imaging in Combination with Elemental Analysis

Although electron beam microanalysis offers excellent methods for quantifying specific elements within an error of <10%, estimating the mass, especially the undamaged mass, of the analyzed microvolume with comparable confidence remains a difficult problem. Yet mass measurements are clearly essential. From a technical viewpoint, the x-ray continuum as a measure of mass underlies the widely accepted Hall method of electron probe microanalysis (Hall and Gupta, 1983). Physiologically speaking, changes in mass and water content are essential aspects of many cell functions. In such cases, precise elemental analysis without knowledge of water and protein changes is not particularly meaningful. Dark-field mass mapping of cryosections at the level of single organelles has the potential to provide exactly the critical information on analyzed mass that is required for both technical and biological reasons. We illustrate a technical application—namely, the correction of EDXS microanalysis data for mass loss and the conversion of dry-weight concentrations to wet-weight concentrations—in the context of understanding intracellular calcium regulation, which is a major function of the endoplasmic reticulum (ER) in many cell types.

The Purkinje cell is a large neuron of the cerebellum with an elaborate, branching dendritic network on which
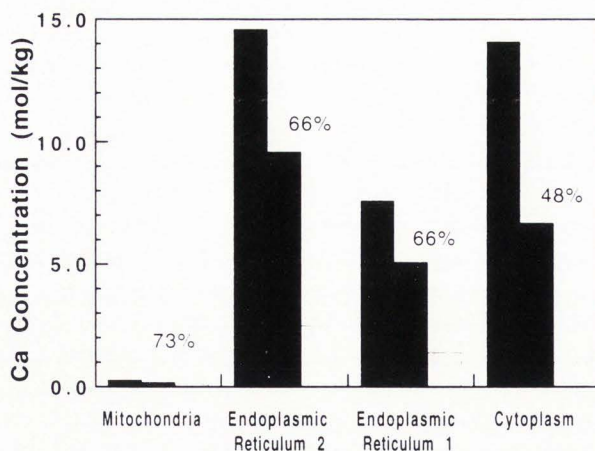
Fig. 9. Calcium concentrations in various compartments of Purkinje cell dendrite. Concentrations in mmol/kg dry weight, extracted directly from multiple-least-squares fitting (black bar), were corrected for mass loss during analysis (gray bars) by multiplying by fraction of mass retained (percentages on plot). Optionally, these can be further converted to wet-weight concentrations (mmol/kg wet weight, white bars) by multiplying by original dry mass fraction. Typical mass data for these organelles are given in Fig. 7; methods of microanalysis and errors of analysis are described in the footnote to Table 2.
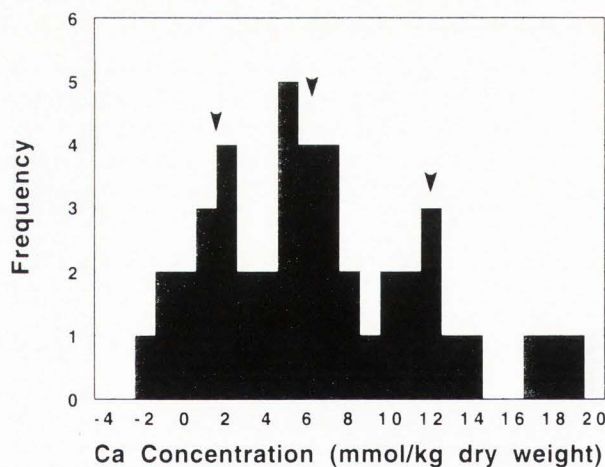

Fig. 10. Distribution of dry-weight total calcium concentrations within endoplasmic reticulum of Purkinje cell dendrites. Data from several dendrites in a single representative section of cerebellar cortex. Arrows indicate means of gaussians empirically fit to this data set. Two rightmost populations have calcium contents indicative of calcium-sequestering organelles.

it receives synaptic input. The strength with which Purkinje cells integrate and transmit this input is critically dependent on changes in intracellular calcium concentration. We have previously used EDXS microanalysis to show that during synaptic activity the ER in Purkinje cell synapses and nearby dendritic branches accumulates and releases substantial amounts of calcium, resulting in characteristic states of ER which could be defined by their calcium content (Andrews *et al.*, 1988). Recent studies have now shown that the ER of these dendrites expresses different types of intracellular calcium release channels (Satoh *et al.*, 1990; Walton *et al.*, 1991) which regulate calcium differently in response to neurotransmitter binding. Current experiments in our laboratory are aimed at identifying and differentiating the subclasses of calcium-sequestering ER that are found in Purkinje cells.

The concentrations of calcium in identified compartments of a single Purkinje cell dendrite (Fig. 3), as determined by established methods of EDXS microanalysis (Hall and Gupta, 1983; Kitazawa *et al.*, 1983) from single 100-s spectra with a *ca.* 5 nA probe current, are shown in Fig. 9. Also shown (Fig. 9 and the last column of Table 2) are the same data after correcting for mass loss by multiplying by the ratio of high-dose mass to low-dose mass, as determined from dark-field intensities and given in Fig. 7. The corrections range from modest (mitochondria) to quite large (cytoplasm), and it is clear that how one interprets the distribution of calcium between these compartments depends on considering the mass corrections. In addition, errors that arise by ignoring mass corrections may be propagated during conversion to wet-weight concentrations (Fig. 9). As a specific example, the data in Fig. 9 demonstrate that there are indeed at least two distinct types of ER that can be distinguished on the basis of their calcium content. The corrected results show that both types have dry-weight and wet-weight calcium concentrations higher than or comparable to the cytoplasm, although this is not obvious from the uncorrected data. In cases where differential mass loss affects the interpretation of experimental results, dark-field mass analysis would seem to be a sensitive and effective method for assessing and correcting for structural damage and mass loss.

Data from several experiments reveal a distribution of calcium concentrations which we presently interpret as two populations of calcium-rich dendritic ER plus a third population which does not appear to sequester calcium (Fig. 10). Concentrations of other elements within these organelles are otherwise similar (Table 2). The mean total calcium concentrations for the calcium-rich populations (two rightmost arrows in Fig. 9) were 6.9 ± 0.4 and 13.3 ± 0.8 mmol/kg dry weight $\pm$ SEM. As

Table 2. Elemental concentrations in organelles of a Purkinje cell dendrite[*]

	Na	Mg	P	S	Cl	K	Ca
			(mmol/kg dry weight with mass loss correction)				
Mitochondria	10.4±3.1	12.4±2.6	187.5±3.7	134.5±3.8	10.4±2.2	211.6±5.8	0.2±1.9
Endoplasmic reticulum 1	6.5±3.6	11.6±3.0	298.9±5.0	100.6±3.8	16.9±2.2	318.5±7.6	5.0±2.4
Endoplasmic reticulum 2	10.5±3.6	15.5±3.0	282.6±4.8	101.7±3.8	22.7±2.4	278.7±7.1	9.6±2.5
Cytoplasm	34.5±6.4	13.0±5.1	198.1±6.8	106.6±6.0	28.9±4.1	440.6±13.4	6.7±4.1

[*] EDXS data acquired from single organelles in one dendrite at -160° C with doses of $> 10^8$ e/nm^2. Concentrations determined from a single 100s EDXS analysis at ≈ 4 nA probe current. Data processing by established procedures and corrected for mass loss as described in text. Errors are uncertainties from multiple-least-squares fit.

the calcium content of the first class of dendritic ER is similar to that of ER known to express the inositol-1,4,5-trisphosphate (IP$_3$) receptor (Bond et al., 1984; Buchanan et al., 1992), this population will likely prove to be IP$_3$-sensitive storage organelles. It is tempting to speculate that the even higher calcium content of the other, less abundant, class may be a signature for ER expressing the ryanodine-sensitive calcium release channel. In this case the presence of two types of ER, representing IP$_3$- and ryanodine-sensitive calcium release channels, in Purkinje cell dendrites would lend support to current ideas regarding the spatial regulation of second-messenger calcium (Burgoyne and Cheek, 1991; Muller and Connor, 1991) by the action of diverse calcium release channels (Walton et al., 1991).

The calcium sensitivity for EDXS analysis of cisterns of ER, both in the STEM and in optimized AEMs, can be quite good, with errors well below a 1.0 mmol/kg dry weight (Somlyo et al., 1985; Leapman and Andrews, 1991); this is equivalent to only a few tens of calcium atoms within the analyzed volume of such a small organelle. Thus, the small probe size and high stability of the HB501 STEM, in combination with high-quality freeze-dried cryosections, make high resolution analysis of 10-nm scale cellular structures possible, subject mainly to radiation damage as the ultimate limit to analytical resolution. It has been demonstrated that parallel-detection EELS offers an advantage in sensitivity over EDXS for analysis of important biological elements such as calcium and phosphorus (Shuman and Somlyo, 1987). Previously it has been difficult to apply EELS at 100 keV beam energy to cryosections because the specimens were too thick and the energy loss spectra were dominated by plural inelastic scattering (Leapman and Ornberg, 1988).

The present cryosections, however, are well under one mean free path in thickness, so we are able to obtain spectra from single organelles with a three- to fourfold improvement in sensitivity over that achievable by EDXS (Leapman et al., 1993). The details of quantitative analysis of cryosections by EELS, including application of the powerful "spectrum-imaging" mapping technique (Hunt and Williams, 1991; Jeanguillaume and Colliex, 1989; Balossier et al., 1991), are discussed in a companion paper (Leapman et al., 1994).

Conclusions

This paper reviews some recently developed capabilities of low-dose dark-field imaging in the field-emission STEM, with emphasis on high-quality ultrathin cryosections of directly frozen tissues. Dark-field images demonstrate that structural detail in these sections can be comparable to conventional thin sections. In addition, the cryosections are thin enough to characterize quantitatively in the STEM, so that established dark-field techniques for mass analysis can be used to measure the mass of individual structures and organelles in situ. The results suggest several new biological applications for dark-field imaging, which are illustrated in the context of understanding synaptic activity-dependent calcium regulation in Purkinje cells of the mouse cerebellar cortex. Thus, we have reported the in situ masses of undamaged dendritic organelles and compartments—ER, mitochondria and cytoplasm—that are thought to be involved in calcium regulation, the effects of electron beam damage on the structure and masses of these same organelles, and the elemental content of these organelles after correction for the damaging effects of analytical electron doses. Elemental analysis provides strong

evidence that the endoplasmic reticulum is the major calcium storage organelle in Purkinje cell dendritic shafts. It further demonstrates that dendritic ER is a compositionally heterogeneous organelle, which is thought to be a consequence of the expression of different calcium-release channels.

Acknowledgments

References

Andrews SB, Gallant PE, Leapman RD, Schnapp BJ, Reese TS (1993) Single kinesin molecules cross-bridge microtubules in vitro. Proc Natl Acad Sci USA **90**: 6503-6507.

Andrews SB, Leapman RD (1989) Performance of a cryotransfer/cold stage system for a VG Microscopes HB501 STEM. Microbeam Analysis-1989, pp 85-88.

Andrews SB, Leapman RD, Landis DM, Reese TS (1988) Activity-dependent accumulation of calcium in Purkinje cell dendritic spines. Proc Natl Acad Sci USA **85**: 1682-1685.

Balossier G, Thomas X , Michel J, Wagner D, Bonnehomme P, Puchelle E, Ploton D, Bonnehomme A, Pinon JM (1991) Parallel EELS elemental mapping in scanning transmission electron microscopy: Use of the difference method. Microsc Microanal Microstruct **2**: 531-546.

Bond M, Shuman H, Somlyo AP, Somlyo AV (1984) Total cytoplasmic calcium in relaxed and maximally contracted rabbit portal vein smooth muscle. J Physiol (Lond) **357**:185-210.

Buchanan RA, Leapman RD, Landis DM, Reese TS, Andrews SB (1992) Calcium regulation by endoplasmic reticulum in Purkinje cell dendrites and dendritic spines. Mol Biol Cell **3**: 32a (abstr).

Buchanan RA, Leapman RD, O'Connell MF, Reese TS, Andrews SB (1993) Quantitative scanning transmission electron microscopy of ultrathin cryo-sections: Subcellular organelles in rapidly frozen liver and cerebellar cortex. J Struct Biol **110**: 244-255.

Burgoyne RD, Cheek TR (1991) Locating intracellular calcium stores. Trends Biol Sci **16**: 319-320.

Colliex C (1985) An illustrated review of various factors governing the high spatial resolution capabilities in EELS microanalysis. Ultramicroscopy **18**: 131-150.

Colliex C, Jeanguillaume C, Mory C (1984) Unconventional modes for STEM imaging of biological structures. J Ultrastruct Res **88**: 177-206.

Crewe AV, Wall J (1970) A scanning microscope with 5 Å resolution. J Mol Biol **48**: 375-393.

Dubochet J, Adrian M, Chang JJ, Homo JC, Lepault J, McDowall AW, Schultz P (1988) Cryo-electron microscopy of vitrified specimens. Q Rev Biophys **21**: 129-228.

Engel A (1978) Molecular weight determination by scanning transmission electron microscopy. Ultramicroscopy **3**: 273-281.

Engel A, Reichelt R (1984) Imaging of biological structures with the scanning transmission electron microscope. J Ultrastruct Res **88**: 105-120.

Fiori CE, Swyt CR (1992) NIST/NIH Desktop Spectrum Analyzer, SRD-38, National Institute of Standards and Technology, Gaithersburg, MD.

Glaeser RM, Zilker A, Radermacher M, Gaub HE, Hartmann T, Baumeister W (1991) Interfacial energies and surface-tension forces involved in the preparation of thin, flat crystals of biological macromolecules for high-resolution electron microscopy. J Microsc **161**: 21-45.

Goldstein LSB (1991) The kinesin superfamily: tails of redundancy. Trends Cell Biol **1**: 93-98.

Gupta BL, Hall TA (1981) The X-ray microanalysis of frozen-hydrated sections in scanning electron microscopy: An evaluation. Tissue & Cell **13**: 623-643.

Hall TA, Gupta BL (1983) The localization and assay of chemical elements by microprobe methods. Q Rev Biophys **16**: 279-339.

Hunt J (1989) Computer-aided parallel EELS techniques: acquisition, processing and imaging. In: *Proc 47th Ann Mtg Electron Microsc Soc America* (Bailey GW, ed) San Francisco Press, San Francisco, pp 398-399.

Hunt J, Williams DB (1991) Electron energy-loss spectrum-imaging. Ultramicroscopy **38**: 47-73.

Isaacson MS (1977) Specimen damage in the electron microscope. In: *Principles and Techniques of Electron Microscopy* (Hayat MA, ed) Van Nostrand Reinhold, New York, pp 1-78.

Isaacson MS, Johnson D (1975) Low Z elemental analysis using energy loss electrons. Ultramicroscopy **1**: 33-52.

Jeanguillaume C, Colliex C (1989) Spectrum-image: the next step in EELS digital acquisition and processing. Ultramicroscopy **28**: 252-257.

Kitazawa T, Shuman H, Somlyo AP (1983) Quantitative electron probe analysis: Problems and solutions. Ultramicroscopy **11**: 251-250.

Krivanek OL, Paterson JH, Poppa HR (1989) Performance of the Gatan PEELS on the VG HB501 STEM. In: *Proc 47th Ann Mtg Electron Microsc Soc*

America (Bailey GW, ed) San Francisco Press, San Francisco, pp 410-411.

Leapman RD, Andrews SB (1991) Analysis of directly frozen macromolecules and tissues in the field-emission STEM. J Microsc **161**: 3-19.

Leapman RD, Andrews SB (1992) Characterization of biological macromolecules by combined mass mapping and electron energy-loss spectroscopy. J Microsc **165**: 225-238.

Leapman RD, Hunt JA, Buchanan RA, Andrews SB (1993) Measurement of low calcium concentrations in cryosectioned cells by parallel-EELS mapping. Ultramicroscopy **49**: 225-234.

Leapman RD, Ornberg RL (1988) Quantitative electron energy loss spectroscopy in biology. Ultramicroscopy **24**: 251-268.

Leapman RD, Sun SQ, Hunt JA, Andrews SB (1994) Biological electron energy loss spectroscopy in the field-emission STEM. Scanning Microsc Suppl **8**: 245-259.

Michel M, Gnägi H, Müller M (1992) Diamonds are a cryosectioner's best friend. J Microsc **166**: 43-56.

Muller W, Connor JA (1991) Dendritic spines as individual neuronal compartments for synaptic Ca^{2+} responses. Nature **354**: 73-76.

Nicholls AW, Bovey PE (1989) A cryotransfer facility for the VG HB501 STEM. In: *Proc 47th Ann Mtg Electron Microsc Soc America* (Bailey GW, ed) San Francisco Press, San Francisco, pp 746-747.

Reichelt R, Engel A (1986) Contrast and resolution of scanning transmission electron microscope imaging modes. Ultramicroscopy **19**: 43-56.

Satoh T, Ross CA, Villa A, Sapattapone S, Pozzan T, Snyder SH, Meldolesi J (1990) The inositol 1,4,5-trisphosphate receptor in cerebellar Purkinje cells: Quantitative immunogold labeling reveals concentrations in an ER subcompartment. J Cell Biol **111**: 615-624.

Shuman H, Somlyo AP (1987) Electron energy loss analysis of near-trace-element concentrations of calcium. Ultramicroscopy **21**: 23-32.

Somlyo AP, Bond M, Somlyo AV (1985) Calcium content of mitochondria and endoplasmic reticulum in liver rapidly frozen in vivo. Nature **314**: 622-625.

Sun S, Shi SL, Leapman RD (1993) Water distributions of hydrated biological specimens by valence electron energy loss spectroscopy. Ultramicroscopy **50**: 127-139.

von Zglinicki T (1991) The measurement of water distribution in frozen specimens. J Microsc **161**: 149-158.

Wall JS (1979) Mass measurements with the electron microscope. Scanning Electron Microscopy 1979; II, 291-302.

Wall JS, Hainfeld JF (1986) Mass mapping with the scanning transmission electron microscope. Ann Rev Biophys Chem **15**: 355-376.

Walton PD, Airey JA, Sutko JL, Beck CF, Mignery GA, Sudhof TC, Deerinck TJ, Ellisman MH (1991) Ryanodine and inositol trisphosphate receptors coexist in avian cerebellar Purkinje neurons. J Cell Biol **113**: 1145-57.

Zierold K (1988) X-ray microanalysis of freeze-dried and frozen hydrated cryosections. J Electron Microsc Tech **9**: 65-82.

Discussion with Reviewers

T. von Zglinicki: Total calcium as measured by x-ray microanalysis is practically 100% bound. Therefore, a calcium-sequestering organelle should be characterized by a significantly increased Ca content per unit weight, not only per volume (= wet mass). Accepting this definition, my interpretation of your data would be that dendritic endoplasmic reticulum does not sequester Ca under your conditions of analysis. If I sum up the data provided in Fig. 10, I end up with an average Ca concentration in the ER of 6.4 ± 5.2 mmol/kg dry weight, which is about the same as the value given for the cytoplasm in Table 2. Please comment!

Authors: We would propose that a practical description of a calcium-sequestering organelle is one which has a calcium pump and a calcium release channel in its membrane, and can accumulate calcium against an electrochemical gradient. Such an organelle does not necessarily have a dry weight calcium concentration much higher than cytoplasm, even when fully calcium loaded. As an illustration, take an organelle with twice the amount of internal calcium, as compared with cytoplasm, in the analyzed volume but also with twice the mass (perhaps due to large amounts of calcium-buffering proteins such as calsequestrin). Such an organelle would have precisely the same calcium concentration as the cytoplasm on a dry-weight basis, but on a wet-weight basis the concentration in the organelle will be twice as high. While this example is somewhat extreme, the data in Fig. 10 reflect a more common situation for calcium-sequestering organelles, which we interpret as follows.

Rather than pool the data, our current view considers this distribution of calcium as representing three distinct physiological states, whose mean concentrations are indicated by the arrows on Fig. 10. One state has a concentration which is similar to normal cytoplasmic values (3.0 mmol/kg dry weight, 17g/100g dry mass, therefore 0.5 mmol/kg wet weight), and therefore represents either a non-sequestering organelle or an

empty sequestering organelle. The other two populations have calcium concentrations which are notably higher than cytoplasm on both a wet- and dry-weight basis, and therefore may be calcium-sequestering organelles.

The data in Table 2 and Fig. 9 are from single analyses of individual organelles in one dendrite. This presentation is intended to give a feeling for the statistical uncertainties associated with a single analysis. The dry weight concentration for cytoplasmic calcium in this particular dendrite is 6.7 ± 4.1 mmol/kg, which converts to 1.0 ± 0.6 mmol/kg wet weight—higher than "typical" cytoplasm, but not significantly so. If this difference were significant, it might be because this is an activated dendrite in which total cytoplasmic calcium has been elevated (approximately twofold) by release from calcium stores or by uptake through calcium channels.

T. von Zglinicki: When we used total tissue wet weight concentrations as internal standards for the determination of local dry mass fractions in, among others, rat liver (von Zglinicki *et al.* (1987) J. Microsc. **146**: 67-76), we realized that the outcome of the calculation would be critically dependent on the volume fractions of all intracellular organelles as well as the extracellular space. There are rather large differences between data obtained in different labs. Where were your volume fraction data taken from and how large are the fraction used in your calculations?

Authors: One nice feature of the dark-field mass analysis method described here is that it does not depend on any assumptions regarding the volume distribution of various cellular compartments; for any two compartments, the ratio of dry mass is simply equal to the ratio of corrected dark-field counts per pixel. To derive absolute dry mass, the method does require the use of some region of the image as a "internal standard" (we used the whole image and assumed that it was representative of the entire tissue whose dry mass was independently known), but relative dry masses are not affected by uncertainties in the standard. The major assumptions of the dark-field method probably are: 1) that the hydrated thickness section is uniform (which is likely to be true for modern cryosections); and 2) that organelle shrinkage during freeze-drying is uniform and non-differential (which is not reliably true).

L. Edelmann: Could you comment on the nature of mass loss upon irradiation of the sections with high electron doses? For example, can you detect the loss of light elements or of water? Is a loss or redistribution of calcium or other elements conceivable? Do you think that mass loss upon irradiation may be reduced after

freeze-drying of the section for prolonged periods at low and high temperatures?

Authors: The mass loss quantified here (Figs. 7 and 9) is entirely due to the loss of light elements, which can be confirmed by directly observing by EELS the loss of light elements during the first high-dose exposures. Even at relatively modest doses, all hydrogen and oxygen is quickly lost, while carbon is essentially retained; nitrogen loss is intermediate. For heavier elements ($Z > 10$), there appears to be no measurable loss under our analysis conditions, as is shown by reproducing the quantitation of heavier elements in subsequent analyses. (Some sulfur is lost during analyses at higher temperatures.) This reproducibility also indicates that significant redistribution of heavier elements is not occurring. Regarding any effects of the freeze-drying protocol on mass loss, we expect that the main role of freeze-drying is to maintain the sections well attached to their support and to ensure that they are completely dry; we and others have shown that mass loss is quite different and much worse when any water is present.

R. Wróblewski: It was difficult to be fully convinced by your description of the kinesin protein (Fig. 1), where you described head, stalk, and tail regions in a structure that occupies approximately 20 pixels and only 6-7 pixels have an intensity significantly above background. Is your description base on numerous images?

Authors: As you have surmised, the quantitative analysis of kinesin—and especially the characterization of protein domains—is based on averaging many images of single molecules. In this sense, mass mapping is an analytical, not a visual, technique. However, we have presented the kinesin image in Fig. 1 to illustrate that after one knows where to look, protein segments as small as coiled-coil α-helices can be seen. We also note that for a molecule the size of kinesin (approximately 350 kD), mass analysis of a single molecule is statistically significant with a precision better than 10%.